Geophys. J. Int. (2004) **157,** 315–331 doi: 10.1111/j.1365-246X.2004.02214.x

Resolution limit of traveltime tomography

F. A. Dahlen

Department of Geosciences, Princeton University, Princeton 08544, *NJ, USA. E-mail: fad@princeton.edu*

Accepted 2003 December 9. Received 2003 December 9; in original form 2003 August 1

SUMMARY

We derive an explicit formula relating a recovered 3-D seismic slowness image to the actual seismic slowness under the assumption that a tomographically complete collection of finite-frequency traveltime shifts is inverted using linearized ray theory. The tomographically recovered image is blunted, or diminished in amplitude, and blurred, or spread laterally, as a result of wave front healing and other finite-frequency diffraction effects. The 1-D spreading varies as the cube root of the amplitude reduction, so that total volume-integrated slowness is conserved.

Key words: integral transforms, inverse theory, tomography, traveltime.

Downloaded from https://academic.oup.com/gji/article/157/1/315/558524 by guest on 22 September 2022

1 INTRODUCTION

Traveltime tomography is a mature seismic exploration method, which has been used to map the 3-D structural details of the earth's interior on a variety of scales from a single oil field to the entire mantle. The resolution and fidelity of tomographic images is marred by three different factors: (i) errors in the measured traveltimes, (ii) uneven or incomplete illumination of the region under study, and (iii) deficiencies in the forward-modelling theory underlying the inversion. One such theoretical deficiency is the almost universal reliance upon seismic ray theory, which is an infinite-frequency approximation. In this ray-theoretical approximation, measured traveltimes are sensitive only to the structure along an infinitesimally thin geometrical ray between the source and receiver. The traveltimes of real, finite-frequency seismic waves are subject to diffraction and wave front healing effects and they are sensitive to 3-D structure off of the geometrical ray. In this paper, we consider the limitations upon tomographic resolution resulting from the finite-frequency character of seismic waves. In doing so, we shall ignore the other two factors that degrade tomographic images: noisy measurements and inadequate ray path coverage. These latter effects are thoroughly addressed in all well-designed tomographic studies through the use of checkerboard tests and other such 'what if' forward-problem simulations. The resolution limit under consideration here is the intrinsic limit resulting from diffraction. We examine this finite-frequency diffraction limit strictly within the context of the linearized traveltime inverse problem. In Section 6 we compare our results with the recent resolution-limit analysis of Sheng & Schuster (2003).

2 STATEMENT OF THE PROBLEM

The highly idealized *gedanken* experiment considered is illustrated in Fig. 1. A smooth, isolated, seismic slowness anomaly $\delta\sigma(\mathbf{x})$ is embedded in an otherwise homogeneous medium, with constant slowness $\sigma(\mathbf{x}) = \sigma$. Two parallel planes, one covered with a dense array of seismic sources and the other with a dense array of receivers, are separated by a distance L, as shown. The 3-D slowness perturbation $\delta\sigma(\mathbf{x})$ is presumed to be slight, compared to the background slowness,

$$|\delta\sigma(\mathbf{x})| \ll \sigma, \tag{1}$$

so that seismic rays do not deviate substantially from the straight lines connecting the sources and receivers. Every source is presumed to be detonated in turn and recorded only by the receiver in the complementary position on the opposing plane. This results in a 2-D sample of traveltime residuals δT, measured with respect to the time $T = \sigma L$ required to traverse the background medium. The source and receiver arrays maintain a fixed position with respect to each other, however, they are presumed to be mounted on giant gimbals enabling such a 2-D sample of traveltime residuals δT to be measured for every possible orientation of the straight ray paths. Thus, the tomographic sampling of the anomaly $\delta\sigma(\mathbf{x})$ by rays of length L is perfect. The measured traveltime residuals δT are presumed to be noise-free.

The residuals are assumed to have been measured by cross-correlation of an observed waveform $s_{\rm obs}(t)$ with the corresponding synthetic waveform $s_{\rm syn}(t)$, computed in the background medium:

$$\int_{t_1}^{t_2} s_{\rm obs}(t) s_{\rm syn}(t - \delta T)\, dt = \text{maximum}, \tag{2}$$

© 2004 RAS

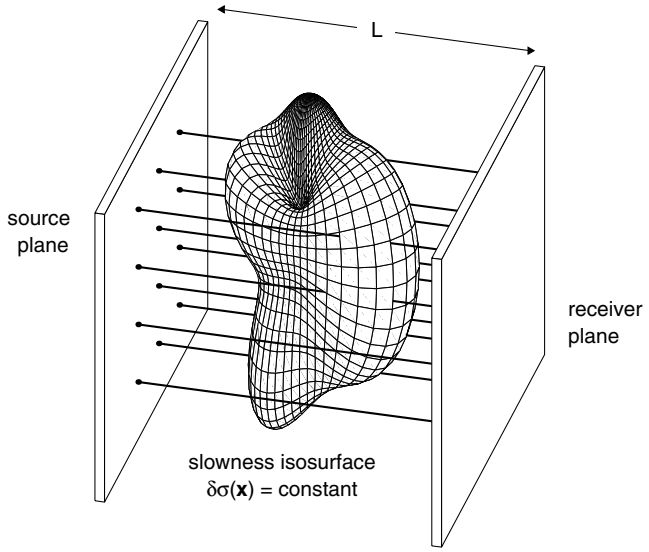

Figure 1. Cartoon illustrating the idealized tomographic inverse problem considered in this paper. A 3-D slowness anomaly $\delta\sigma(\mathbf{x})$, depicted here by a peanut-shell-shaped isosurface, is sampled by a family of straight, parallel seismic rays, depicted by heavy solid lines. The rays are of equal length L and the source and receiver arrays are distributed continuously over their respective planes. The planes can be rotated to all possible angular orientations, so that the tomographic sampling of the anomaly is perfect. We seek to recover the 3-D slowness distribution $\delta\sigma(\mathbf{x})$ from the infinite suite of measured traveltime residuals δT.

where the time window, $t_1 \le t \le t_2$, is chosen to include the entire synthetic pulse. If the medium is an acoustic fluid and the receivers record pressure variations, the synthetic response is given by (Morse & Ingard 1968)

$$s_{\rm syn}(t) = \frac{\rho \dot{m}(t - \sigma L)}{4\pi L}, \tag{3}$$

where ρ is the fluid density, $m(t)$ is the instantaneous rate of change of an infinitesimally small volume situated at the source and the dot denotes differentiation with respect to time. Upon linearization of eq. (2), we obtain a first-order relation between the cross-correlation traveltime shift δT and the 3-D slowness anomaly $\delta\sigma(\mathbf{x})$:

$$\delta T = \int\int\int_{-\infty}^{\infty} K(\mathbf{x})\, \delta\sigma(\mathbf{x})\, d^3\mathbf{x}. \tag{4}$$

Throughout this paper, we shall consider integrals such as that in eq. (4) to be over all of space, $\|\mathbf{x}\| < \infty$; in practice, the integration can obviously be confined to the region in which $\delta\sigma(\mathbf{x}) \neq 0$. The quantity $K(\mathbf{x})$ is the Fréchet kernel expressing the sensitivity of the finite-frequency traveltime measurement δT to the slowness perturbation at the point $\mathbf{x}$. In the case of a homogeneous background medium, this kernel is given, exactly, by (Dahlen *et al.* 2000; Hung *et al.* 2001)

$$K(\mathbf{x}) = \frac{\sigma}{2\pi} \left(\frac{L}{L' L''} \right) \frac{\int_0^\infty \omega^3 |\dot{m}(\omega)|^2 \sin(\omega \Delta T)\, d\omega}{\int_0^\infty \omega^2 |\dot{m}(\omega)|^2 d\omega}, \tag{5}$$

where L' and L' are the source-to-scatterer and scatterer-to-receiver distances, as shown in the top of Fig. 2. The presence in eq. (5) of the normalized power spectrum $|\dot{m}(\omega)|^2$ serves as a reminder that this is the Fréchet kernel for a finite-frequency traveltime measured by cross-correlation with a broad-band synthetic pulse ($s_{\rm syn}(t)$), composed of waves having all angular frequencies ω. The quantity

$$\Delta T = \sigma(L' + L'' - L) \tag{6}$$

is the additional time required for a wave to travel the dog-leg path from the source to the scatterer $\mathbf{x}$ to the receiver, rather than taking the straight source-to-receiver path. The results (eqs 4–6) are obtained by invoking the Born approximation, which ignores all but single-scattering interactions.

A cross-section through a typical traveltime Fréchet kernel $K(\mathbf{x})$ is shown in the bottom of Fig. 2. It is noteworthy that the sensitivity is identically zero everywhere along the geometrical ray (Dahlen *et al.* 2000; Zhao *et al.* 2000). This feature, together with the familiar upward curvature of seismic rays within a spherically symmetric earth, has given rise to the whimsical terminology banana-doughnut kernel; in the homogeneous-background case under consideration here, a hollow cucumber or zucchini might be a more appropriate culinary metaphor. The source-pulse power spectrum $|\dot{m}(\omega)|^2$ used to plot the sensitivity kernel $K(\mathbf{x})$ in Fig. 2 is given by

$$|\dot{m}(\omega)|^2 = (\omega^2 \sigma^2 \lambda^2 / 2\pi) \exp(-\omega^2 \sigma^2 \lambda^2 / 4\pi^2). \tag{7}$$

The parameter λ is the characteristic wavelength of the waves comprising the pulse. We shall use the simple analytical spectrum (eq. 7) for illustrative purposes throughout this paper.

Downloaded from https://academic.oup.com/gji/article/157/1/315/558524 by guest on 22 September 2022

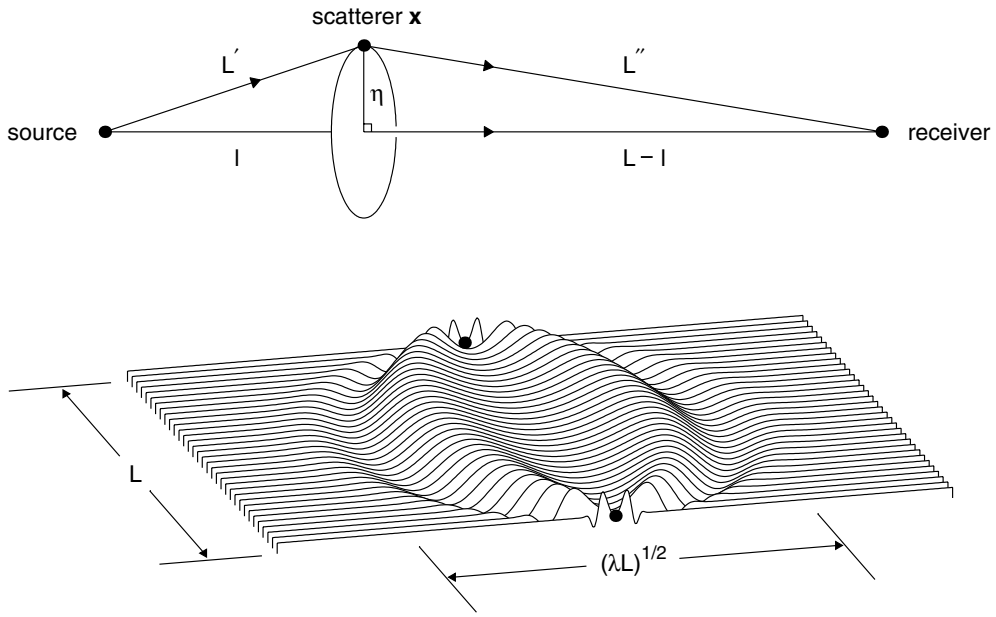

Figure 2. (Top) Geometrical notation used in the specification of the traveltime Fréchet kernel $K(\mathbf{x})$. Every single scatterer $\mathbf{x}$ is projected onto the nearest point on the straight-line source-to-receiver ray. Distance along the ray is denoted by l and distance perpendicular to the ray is denoted by η. The distances L' and L' are measured from the source to the scatterer and from the scatterer to the receiver, respectively. (Bottom) Foreshortened perspective view of a longitudinal cross-section through the sensitivity kernel $K(\mathbf{x})$. Black dots show the locations of the source and receiver; the path length in this example is $L = 20\lambda$, where λ is the characteristic wavelength. A measured traveltime residual δT is maximally sensitive to slowness variations $\delta\sigma(\mathbf{x})$ in a circularly symmetric cucumber skin surrounding the source-to-receiver ray. The diameter of the region of significant traveltime sensitivity is $\sqrt{\lambda L}$, measured at the midpoint of the ray.

It is now possible to give a precise statement of the problem that will be solved in this paper. We assume that the measured traveltime residuals δT are adequately described by the linearized relation (eqs 4–5), however, that they are inverted using the corresponding linearized ray-theoretical relation

$$\delta T_{\text{ray}} = \int_0^L \delta\sigma(\mathbf{x})\, dl, \tag{8}$$

where the 1-D integral is evaluated along the straight source-to-receiver ray. How is the recovered image, which we shall denote by $\delta\hat{\sigma}(\mathbf{x})$, related to the actual image $\delta\sigma(\mathbf{x})$, assuming that the ray coverage is tomographically complete, as described above?

To expedite the analysis, we shall restrict consideration to a slowness anomaly $\delta\sigma(\mathbf{x})$ whose characteristic spatial dimension a is small compared with the source-receiver distance,

$$a \ll L, \tag{9}$$

and we shall assume that the anomaly is situated approximately midway between the source and receiver:

$$L' \approx L'' \approx L/2. \tag{10}$$

The detour traveltime (eq. 6) can, in this case, be approximated by the first term in a paraxial expansion:

$$\Delta T \approx \left(\frac{2\sigma}{L}\right)\eta^2, \tag{11}$$

where η is the perpendicular distance from the ray to the scatterer $\mathbf{x}$, as illustrated in the top of Fig. 2. In this approximation, the sensitivity kernel $K(\mathbf{x})$ is independent of the distance l along the ray and a function only of the path-perpendicular offset η:

$$K(\eta) = \frac{2\sigma}{\pi L N}\int_0^\infty \omega^3 |\dot{m}(\omega)|^2 \sin\left(\frac{2\omega\sigma}{L}\eta^2\right) d\omega, \tag{12}$$

where we have introduced a shorthand notation for the normalization integral in the denominator of eq. (5):

$$N = \int_0^\infty \omega^2 |\dot{m}(\omega)|^2\, d\omega. \tag{13}$$

The approximation (eq. 12) substantially simplifies the 3-D integration over the scatterer location $\mathbf{x}$ in eq. (4). It is noteworthy that we do not impose any restriction upon the spatial extent of the slowness anomaly $\delta\sigma(\mathbf{x})$ relative to the mid-ray diameter $\sqrt{\lambda L}$ of the region of significant traveltime sensitivity: the only restriction is that the anomaly must be small compared with the source-receiver ray length L.

The extent to which wave front healing and other finite-frequency diffraction phenomena affect traveltime measurements δT is governed by the dimensionless ratio

$$d = \frac{a}{\sqrt{\lambda L}}. \tag{14}$$

Downloaded from https://academic.oup.com/gji/article/157/1/315/558524 by guest on 22 September 2022

Physically, d is a measure of how well the anomaly $\delta\sigma(\mathbf{x})$ fits into the insensitive hollow region of the kernel $K(\mathbf{x})$; following Baig *et al.* (2003), we shall refer to the ratio (eq. 14) as the doughnut-hole parameter. Whenever the spatial size of the anomaly is large compared with the width of the kernel, we expect ray theory to be valid, and, indeed, Baig & Dahlen (2004) have verified that eqs (4)–(5) reduce, exactly, to eq. (8): $\delta T \to \delta T_{\rm ray}$ in the limit $d \to \infty$. It is well known that inversion of a tomographically complete suite of ray-theoretical traveltimes $\delta T_{\rm ray}$ will result in an artifact-free recovered image: $\delta\hat{\sigma}(\mathbf{x}) \to \delta\sigma(\mathbf{x})$ in the limit $d \to \infty$. For a complete suite of finite-frequency traveltimes δT, characterized by finite values of d, the recovered image will be imperfect: $\delta\hat{\sigma}(\mathbf{x}) \neq \delta\sigma(\mathbf{x})$. The question is: how can we characterize this diffraction-induced blunting and blurring?

3 MATHEMATICAL REVIEW

We begin with a brief review of some classical mathematical results, intended primarily to establish a convenient notation. In particular, we introduce two well-known integral transformations that will play a critical role in the analysis.

3.1 Radon transform

Let $f(\mathbf{x})$ be an arbitrary real, scalar-valued function defined in a connected region of 3-D space, and let

$$P = (\mathbf{x} : p = \hat{\mathbf{p}} \cdot \mathbf{x}) \tag{15}$$

be a plane passing through this region, as shown in Fig. 3. The 3-D Radon transform of $f(\mathbf{x})$ is the 2-D integral over this plane:

$$f_{\rm R}(p, \hat{\mathbf{p}}) = \int\int_P f(\mathbf{x})\, d^2\mathbf{x}. \tag{16}$$

As indicated, it is convenient to regard $f_{\rm R}(p, \hat{\mathbf{p}})$ as a function of two variables: the offset p of the plane P from a parallel plane through the origin, and the orientation of P, as specified by its unit normal $\hat{\mathbf{p}}$. Knowledge of $f_{\rm R}(p, \hat{\mathbf{p}})$ for all possible offsets p and orientations $\hat{\mathbf{p}}$ enables us to reconstruct the original function $f(\mathbf{x})$ via the inverse Radon transform,

$$f(\mathbf{x}) = -\frac{1}{8\pi^2} \int\int_\Omega \partial_p^2 f_{\rm R}(p = \hat{\mathbf{p}} \cdot \mathbf{x}, \hat{\mathbf{p}})\, d^2\hat{\mathbf{p}}, \tag{17}$$

where $\Omega = \{\hat{\mathbf{p}} : \|\hat{\mathbf{p}}\|^2 = 1\}$ denotes the unit sphere. It is noteworthy that $f(\mathbf{x})$ is determined by the 2-D integral information on all planes P passing through the point $\mathbf{x}$. The second partial derivative ∂_p^2 must be computed prior to evaluation of $f_{\rm R}(p, \hat{\mathbf{p}})$ at $p = \hat{\mathbf{p}} \cdot \mathbf{x}$ and integration over all angular orientations $\hat{\mathbf{p}}$.

To verify the result (eq. 17) we rewrite the integral over the plane P in eq. (16) as an integral over all of 3-D space by introducing a Dirac delta function:

$$f_{\rm R}(p, \hat{\mathbf{p}}) = \int\int\int_{-\infty}^{\infty} \delta(p - \hat{\mathbf{p}} \cdot \mathbf{y}) f(\mathbf{y})\, d^3\mathbf{y} = \frac{1}{2\pi} \int\int\int_{-\infty}^{\infty} d^3\mathbf{y} \int_{-\infty}^{\infty} d\omega\, e^{i\omega(p - \hat{\mathbf{p}}\cdot\mathbf{y})} f(\mathbf{y}). \tag{18}$$

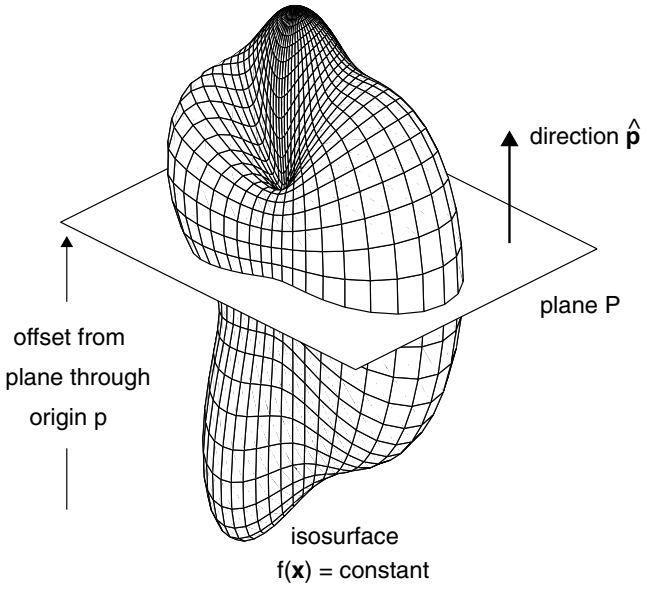

Figure 3. Cartoon illustrating the geometrical character of the 3-D Radon transform $f_{\rm R}(p, \hat{\mathbf{p}})$ of a function $f(\mathbf{x})$. The arguments p and $\hat{\mathbf{p}}$ specify the offset from the origin and the angular orientation of the plane $P = \{\mathbf{x} : p = \hat{\mathbf{p}} \cdot \mathbf{x}\}$, respectively.

Downloaded from https://academic.oup.com/gji/article/157/1/315/558524 by guest on 22 September 2022

Upon taking the ∂_p^2 derivative of eq. (18), inserting the result into eq. (17) and interchanging the order of integration, we obtain

$$f(\mathbf{x}) = \frac{1}{8\pi^3} \int\int\int_{-\infty}^{\infty} d^3\mathbf{y} \int\int_{\Omega} d^2\hat{\mathbf{p}} \int_0^{\infty} d\omega\, \omega^2 e^{i\omega\hat{\mathbf{p}}\cdot(\mathbf{x}-\mathbf{y})} f(\mathbf{y}), \tag{19}$$

where we have exploited the symmetry of the integrand to limit the innermost integral to positive angular frequencies, $0 \le \omega \le \infty$. Upon making the substitution $\mathbf{k} = \omega\hat{\mathbf{p}}$ and noting that $\omega^2\, d\omega\, d^2\hat{\mathbf{p}} = d^3\mathbf{k}$, we can rewrite eq. (19) in the form

$$f(\mathbf{x}) = \int\int\int_{-\infty}^{\infty} d^3\mathbf{y} \left[\frac{1}{8\pi^3} \int\int\int_{-\infty}^{\infty} d^3\mathbf{k} e^{-i\mathbf{k}\cdot(\mathbf{y}-\mathbf{x})} \right] f(\mathbf{y}). \tag{20}$$

The quantity in brackets is the 3-D Fourier representation of the Dirac delta function,

$$\delta(\mathbf{y}-\mathbf{x}) = \frac{1}{8\pi^3} \int\int\int_{-\infty}^{\infty} e^{-i\mathbf{k}\cdot(\mathbf{y}-\mathbf{x})}\, d^3\mathbf{k}, \tag{21}$$

so that eq. (19) reduces to an identity:

$$f(\mathbf{x}) = \int\int\int_{-\infty}^{\infty} \delta(\mathbf{y}-\mathbf{x}) f(\mathbf{y})\, d^3\mathbf{y} = f(\mathbf{x}). \tag{22}$$

This confirms that eqs (16) and (17) are a 3-D integral transform pair; the above proof is a reproduction of that given by Miller *et al.* (1987).

3.2 Abel transform

The Abel transform of a scalar-valued function $f(r)$ of a single real variable r is defined by

$$f_{\mathrm{A}}(q) = \int_{-\infty}^{\infty} f(\sqrt{q^2+l^2})\, dl = 2\int_q^{\infty} \frac{r f(r)\, dr}{\sqrt{r^2-q^2}}. \tag{23}$$

The corresponding inverse Abel transform is (Bracewell 1965)

$$f(r) = -\frac{1}{\pi} \int_r^{\infty} \frac{f'_{\mathrm{A}}(q)\, dq}{\sqrt{q^2-r^2}}, \tag{24}$$

where a prime denotes differentiation with respect to the argument. To verify these relations we differentiate eq. (23),

$$f'_{\mathrm{A}}(q) = 2q \int_q^{\infty} \frac{f'(r)\, dr}{\sqrt{r^2-q^2}}, \tag{25}$$

substitute the result into eq. (24) and interchange the order of integration:

$$\begin{aligned} f(r) &= -\frac{2}{\pi} \int_r^{\infty} \frac{q\, dq}{\sqrt{q^2-r^2}} \int_q^{\infty} \frac{f'(u)\, du}{\sqrt{u^2-q^2}} \\ &= -\frac{2}{\pi} \int_r^{\infty} f'(u)\, du \int_r^{u} \frac{q\, dq}{\sqrt{q^2-r^2}\sqrt{u^2-q^2}}. \end{aligned} \tag{26}$$

The interior integral is elementary,

$$\int_r^{u} \frac{q\, dq}{\sqrt{q^2-r^2}\sqrt{u^2-q^2}} = \frac{\pi}{2}, \tag{27}$$

so that eq. (26) reduces to

$$f(r) = -\int_r^{\infty} f'(u)\, du = f(r). \tag{28}$$

This confirms that eqs (23) and (24) are a 1-D integral transform pair.

3.3 Radon–Abel relations

The Abel transform arises naturally in applications of the 3-D Radon transform $\leftrightarrow$ inverse transform relationship (eqs 16–17) to spherically-symmetric functions of the form

$$f(\mathbf{x}) = f(r) \text{ only}, \quad \text{where } r = \|\mathbf{x}\|. \tag{29}$$

It is evident that the Radon transform (eq. 16) of such a spherically-symmetric function is independent of the orientation $\hat{\mathbf{p}}$ of the plane P:

$$f_{\mathrm{R}}(p, \hat{\mathbf{p}}) = f_{\mathrm{R}}(p) \text{ only}. \tag{30}$$

Downloaded from https://academic.oup.com/gji/article/157/1/315/558524 by guest on 22 September 2022

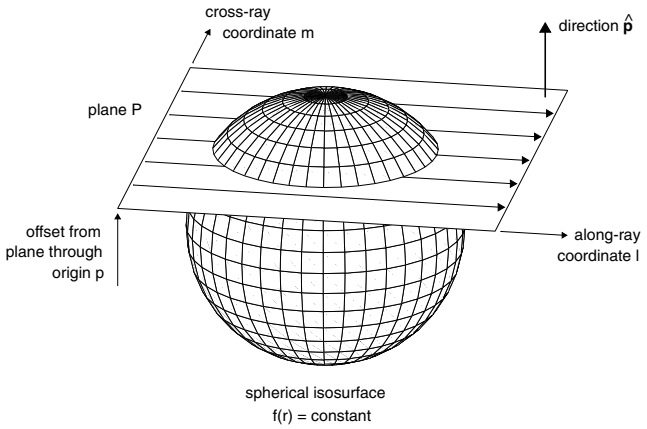

Figure 4. The 3-D Radon transform $f_{\rm R}(p)$ of a spherically-symmetric function $f(r)$ is independent of the orientation $\hat{\mathbf{p}}$ of the plane P. Points $\mathbf{x}$ on the plane P can be described using the three Cartesian coordinates l, m, p. The 2-D integral $f_{\rm R}(p)$ can be evaluated by first integrating with respect to $-\infty \le l \le \infty$ along a ray and then adding the contributions from all rays by integration over $-\infty \le m \le \infty$. The value of $f_{\rm R}(p)$ does not depend upon the orientation of the in-plane coordinates l, m.

As illustrated in Fig. 4, we can compute the 2-D integral of $f(r)$ over an offset plane P using an orthogonal system of along-ray and cross-ray coordinates l, m. The orientation on the plane of l, m may be chosen arbitrarily. The 1-D Radon transform (eq. 30) is given by

$$\begin{aligned} f_{\rm R}(p) &= \int_{-\infty}^{\infty}\int_{-\infty}^{\infty} f(\sqrt{p^2+l^2+m^2})\,dl\,dm \\ &= \int_{-\infty}^{\infty} f_{\rm A}(\sqrt{p^2+m^2})\,dm \\ &= 2\int_{p}^{\infty} \frac{q f_{\rm A}(q)\,dq}{\sqrt{q^2-p^2}}, \end{aligned} \tag{31}$$

where we have substituted $r^2 = p^2 + l^2 + m^2$ and evaluated the resulting integral over r to obtain the second relation. Eq. (31) stipulates that $f_{\rm R}(p)$ is the double Abel transform of $f(r)$, a relationship which may be expressed using an obvious shorthand notation:

$$f_{\rm R}(p) = f_{\rm AA}(p). \tag{32}$$

A single Abel transform $f_{\rm A}(q)$ in this 3-D context can be interpreted as a 1-D line integral (eq. 23) of $f(r)$ along a ray R that is offset from the origin by a distance q, as illustrated in the top left of Fig. 5; the second Abel transform in eqs (31) and (32) accounts for the integration over all rays m on the plane P, as illustrated in the top right of Fig. 5.

Upon writing the concatenated Abel transformation (eq. 32) out in full and interchanging the order of integration, we obtain a much simpler representation of the spherically-symmetric Radon transform:

$$f_{\rm R}(p) = 2\pi \int_{p}^{\infty} r f(r)\,dr, \tag{33}$$

where we have again used the identity (eq. 27). The inverse of eq. (33) is obviously

$$f(r) = -\frac{f_{\rm R}'(r)}{2\pi r}. \tag{34}$$

We can alternatively obtain the simple relation (eq. 34) by specializing the 3-D inverse Radon transform (eq. 17) to the case of a spherically-symmetric function (eq. 29). The orientation $\hat{\mathbf{p}}$ of a plane P passing through a point $\mathbf{x}$ can be parametrized in that case by a single angle $0 \le \theta \le \pi$, as illustrated in the bottom of Fig. 5. The offset of the plane from the origin is $p = r\cos\theta$ and the differential solid angle is $d^2\hat{\mathbf{p}} = 2\pi \sin\theta d\theta$, so that eq. (17) reduces to

$$f(r) = -\frac{1}{4\pi}\int_0^{\pi} \sin\theta f_{\rm R}''(p = r\cos\theta)\,d\theta = -\frac{1}{4\pi r}\int_{-r}^{r} f_{\rm R}''(p)\,dp = -\frac{f_{\rm R}'(r)}{2\pi r}. \tag{35}$$

4 SPHERICALLY-SYMMETRIC SLOWNESS ANOMALY

We begin our diffraction-limit analysis by considering the case of a spherically-symmetric slowness anomaly of the form

$$\delta\sigma(\mathbf{x}) = \delta\sigma(r) \text{ only}, \quad \text{where } r = \|\mathbf{x}\|. \tag{36}$$

The more general case of an arbitrary 3-D slowness anomaly $\delta\sigma(\mathbf{x})$ will be treated in Section 5.

Downloaded from https://academic.oup.com/gji/article/157/1/315/558524 by guest on 22 September 2022

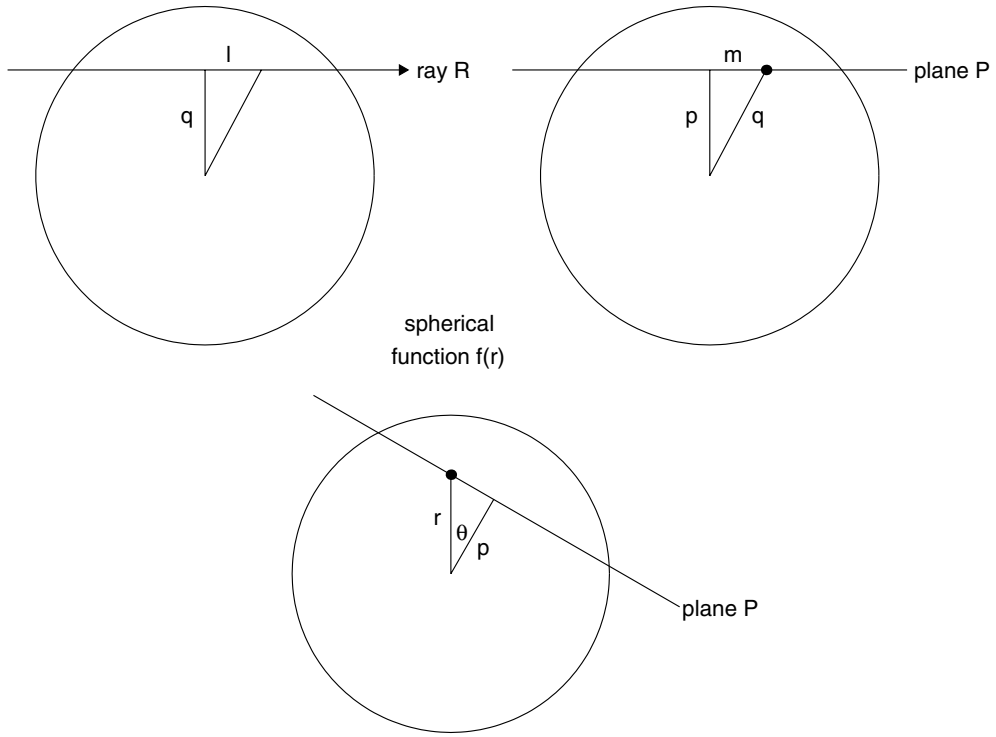

Figure 5. (Top left) The Abel transform $f_{\rm A}(q)$ of a spherically-symmetric function $f(r)$ is the 1-D integral along a ray R of impact parameter q. (Top right) The double Abel or 3-D Radon transform $f_{\rm AA}(r) = f_{\rm R}(r)$ involves an additional cross-ray integration over $-\infty \le m \le \infty$. An individual ray of impact parameter $q = \sqrt{p^2 + m^2}$ is depicted in this view by a dot. (Bottom) Reconstruction of the original function $f(r)$ from its Radon transform $f_{\rm R}(p)$ requires integration over all planes P passing through the observation point, depicted here by a dot. In the spherically symmetric case, a single angle $0 \le \theta \le \pi$ is sufficient to specify the orientation $\hat{\mathbf{p}}$ of the plane.

4.1 Ray-theoretical traveltimes

The ray-theoretical traveltime residual along a seismic ray that is offset by a distance q from the origin is the Abel transform of the slowness distribution $\delta\sigma(r)$:

$$\delta T_{\rm ray}(q) = \int_{-\infty}^{\infty} \delta\sigma(\sqrt{q^2 + l^2})\, dl = 2\int_q^{\infty} \frac{r\delta\sigma(r)\, dr}{\sqrt{r^2 - q^2}} = \delta\sigma_{\rm A}(q). \tag{37}$$

The inverse Abel transform (eq. 24) enables the slowness to be completely recovered from a 1-D suite of traveltime residuals collected at all possible impact parameters, $0 \le q \le \infty$:

$$\delta\sigma(r) = -\frac{1}{\pi}\int_r^{\infty} \frac{\delta T'_{\rm ray}(q)\, dq}{\sqrt{q^2 - r^2}}. \tag{38}$$

In the straight-ray approximation, this relation provides the basis for the determination of the refractivity profiles of planetary atmospheres from radio occultation observations (e.g. Ahmad & Tyler 1998).

Eqs (32) and (37) together stipulate that the Abel transform of the traveltime distribution $\delta T_{\rm ray}(q)$ is the Radon transform of the slowness perturbation:

$$\delta T_{\rm ray,A}(p) = \int_{-\infty}^{\infty} \delta T_{\rm ray}(\sqrt{p^2 + m^2})\, dm = 2\int_p^{\infty} \frac{q\delta T_{\rm ray}(q)\, dq}{\sqrt{q^2 - p^2}} = \delta\sigma_{\rm R}(p). \tag{39}$$

Using eq. (34), we obtain an alternative expression for the tomographically recovered image:

$$\delta\sigma(r) = -\frac{\delta\sigma'_{\rm R}(r)}{2\pi r} = -\frac{\delta T'_{\rm ray,A}(r)}{2\pi r}. \tag{40}$$

This spherically-symmetric version of the 3-D inverse Radon transform is more convenient than the more familiar 1-D Abel inverse (eq. 38) in the present application.

4.2 Traveltime area and anomaly mass

The cross-sectional area of the circularly-symmetric traveltime distribution $\delta T_{\rm ray}(q)$ in the receiver plane is given by

$$2\pi\int_0^{\infty} q\delta T_{\rm ray}(q)\, dq = 4\pi\int_0^{\infty} dq q\int_q^{\infty} \frac{r\delta\sigma(r)\, dr}{\sqrt{r^2 - q^2}} = 4\pi\int_0^{\infty} r^2\delta\sigma(r)\, dr, \tag{41}$$

Downloaded from https://academic.oup.com/gji/article/157/1/315/558524 by guest on 22 September 2022

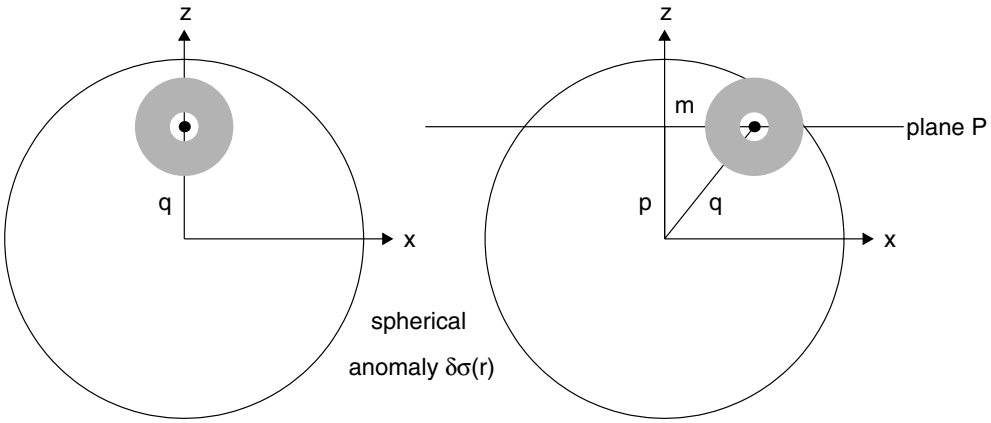

Figure 6. (Left) Geometry used to compute the finite-frequency traveltime residual $\delta T(q)$ through a spherically symmetric slowness anomaly $\delta\sigma(r)$. Dot depicts the ray of impact parameter q; surrounding grey doughnut is a schematic depiction of the surrounding 3-D sensitivity kernel $K(\sqrt{x^2+(z-p)^2})$. (Right) Computation of the Abel transform $\delta T_{\rm A}(p)$ requires an additional integration over all rays $-\infty \le m \le \infty$ on a plane P. Grey doughnut shows the 3-D kernel $K(\sqrt{(x-m)^2+(z-p)^2})$ surrounding an offset ray. The diameter of the anomaly in this pictorial example is substantially larger than the cross-path diameter of the kernel, $a \gg \sqrt{\lambda L}$. The analysis is, however, independent of the magnitude of the ratio $d = a/\sqrt{\lambda L}$.

where we have interchanged the order of integration and evaluated the integral over q to obtain the final relation. The quantity on the right side of eq. (41) is the volume integral of the spherically-symmetric 3-D slowness perturbation $\delta\sigma(r)$: for brevity, we shall refer to this as the anomaly mass in what follows.

4.3 Finite-frequency traveltimes

Suppose now that the ray-theoretical traveltime residuals $\delta T_{\rm ray}$ are replaced by the corresponding finite-frequency traveltime residuals δT, computed using eq. (4). The traveltime residual $\delta T(q)$ along a ray with impact parameter q is given in terms of the approximate 3-D Fréchet sensitivity kernel (eq. 12) by

$$\delta T(q) = \int\int\int_{-\infty}^{\infty} K(\sqrt{x^2+(z-q)^2})\,\delta\sigma(\sqrt{x^2+y^2+z^2})\,dx\,dy\,dz, \tag{42}$$

where x, y, z are a system of Cartesian coordinates, with the ray aligned along the y-axis and passing through the z-axis, as shown on the left side of Fig. 6. The 3-D integral (eq. 42) can be reduced by first using the substitution $r^2 = x^2+y^2+z^2$ to eliminate the along-ray variable y, then substituting $x = u\cos\phi$, $z = u\sin\phi$ and evaluating the integral over the 2-D polar angle ϕ. The result of these manipulations is

$$\delta T(q) = \frac{8\sigma}{LN}\int_0^{\infty} d\omega\,\omega^3|\dot m(\omega)|^2 \int_0^{\infty} du\,u\sin\left[\frac{2\omega\sigma}{L}(q^2+u^2)\right] J_0\left(\frac{4\omega\sigma}{L}qu\right)\int_u^{\infty}\frac{r\,\delta\sigma(r)\,dr}{\sqrt{r^2-u^2}}\,, \tag{43}$$

where N is the normalization integral (eq. 13) and $J_0(z)$ is the Bessel function of order zero. The innermost integral in eq. (43) is one-half times the Abel transform of the slowness anomaly: this enables us to express $\delta T(q)$ in terms of the corresponding ray-theoretical traveltime residual $\delta T_{\rm ray}(q)$, using the relation (37) to give

$$\delta T(q) = \int_0^{\infty} H(q,q')\,\delta T_{\rm ray}(q')\,dq', \tag{44}$$

where

$$H(q,q') = \frac{4\sigma q'}{LN}\int_0^{\infty}\omega^3|\dot m(\omega)|^2\sin\left[\frac{2\omega\sigma}{L}(q^2+q'^2)\right]J_0\left(\frac{4\omega\sigma}{L}qq'\right)d\omega. \tag{45}$$

By interchanging the order of integration in eq. (43), we can express $\delta T(q)$ in an analogous manner in terms of $\delta\sigma(r)$:

$$\delta T(q) = \int_0^{\infty} Q(q,r)\,\delta\sigma(r)\,dr, \tag{46}$$

where

$$Q(q,r) = \frac{8\sigma r}{LN}\int_0^{\infty}\omega^3|\dot m(\omega)|^2\int_0^{r}\frac{\sin\left[\frac{2\omega\sigma}{L}(q^2+u^2)\right]J_0\left(\frac{4\omega\sigma}{L}qu\right)}{\sqrt{r^2-u^2}}\,du\,d\omega. \tag{47}$$

Referring to the right side of Fig. 6, we compute the Abel transform of the traveltime residual,

$$\delta T_{\rm A}(p) = \int_{-\infty}^{\infty}\delta T(\sqrt{p^2+m^2})\,dm = 2\int_p^{\infty}\frac{q\,\delta T(q)\,dq}{\sqrt{q^2-p^2}}, \tag{48}$$

by integrating over all rays m on a plane P offset from the origin by a distance p:

$$\delta T_{\rm A}(p) = \int_{-\infty}^{\infty} dm\int\int\int_{-\infty}^{\infty} K(\sqrt{(x-m)^2+(z-p)^2})\,\delta\sigma(\sqrt{x^2+y^2+z^2})\,dx\,dy\,dz. \tag{49}$$

Downloaded from https://academic.oup.com/gji/article/157/1/315/558524 by guest on 22 September 2022

Eq. (49) can be reduced by first evaluating the integral over m and then using the substitution $r^2 = x^2 + y^2 + z^2$ to eliminate x and y simultaneously:

$$\delta T_{\rm A}(p) = \frac{4\pi}{N}\sqrt{\frac{2\sigma}{\pi L}}\int_0^\infty d\omega\,\omega^{5/2}|\dot m(\omega)|^2\int_0^\infty dz\cos\left[\frac{2\omega\sigma}{L}(p^2+z^2)-\frac{\pi}{4}\right]\cos\left(\frac{4\omega\sigma}{L}pz\right)\int_z^\infty r\delta\sigma(r)\,dr. \tag{50}$$

Upon interchanging the order of integration, we can rewrite this result in the alternative form, analogous to eq. (46):

$$\delta T_{\rm A}(p) = \int_0^\infty P(p,r)\,\delta\sigma(r)\,dr, \tag{51}$$

where

$$P(p,r) = \frac{4\pi r}{N}\sqrt{\frac{2\sigma}{\pi L}}\int_0^\infty \omega^{5/2}|\dot m(\omega)|^2\int_0^r \cos\left[\frac{2\omega\sigma}{L}(p^2+z^2)-\frac{\pi}{4}\right]\cos\left(\frac{4\omega\sigma}{L}pz\right)\,dz\,d\omega. \tag{52}$$

It is noteworthy that eqs (50) and (51)–(52) are simpler than their counterparts eqs (43) and (46)–(47), despite an additional initial integration.

4.4 Recovered image

It is now a straightforward matter to find the recovered spherically-symmetric slowness perturbation $\delta\hat\sigma(r)$ under the assumption that a tomographically complete suite of finite-frequency traveltime residuals $\delta T(q)$ is inverted using ray theory. Adopting a 3-D Radon transform perspective, we define $\delta\hat\sigma(r)$ by the finite-frequency analogue of eq. (40):

$$\delta\hat\sigma(r) = -\frac{\delta\hat\sigma_{\rm R}'(r)}{2\pi r} = -\frac{\delta T_{\rm A}'(r)}{2\pi r} = -\frac{1}{2\pi r}\int_0^\infty \partial_r P(r,r')\,\delta\sigma(r')\,dr'. \tag{53}$$

Upon using eq. (52) to compute the partial derivative $\partial_r P(r,r')$ and evaluating the resulting integral over z, we obtain

$$\delta\hat\sigma(r) = \int_0^\infty G(r,r')\,\delta\sigma(r')\,dr', \tag{54}$$

where

$$G(r,r') = \frac{2}{N}\sqrt{\frac{2\sigma}{\pi L}}\left(\frac{r'}{r}\right)\int_0^\infty \omega^{5/2}|\dot m(\omega)|^2\sin\left[\frac{2\omega\sigma}{L}(r^2+r'^2)-\frac{\pi}{4}\right]\sin\left(\frac{4\omega\sigma}{L}rr'\right)\,d\omega. \tag{55}$$

The quantity $G(r, r')$ can be regarded as a filter, which acts upon the actual image $\delta\sigma(r)$ to form the blunted and blurred image $\delta\hat\sigma(r)$. This finite-frequency, spherically-symmetric blurring filter depends upon the path length L and the power spectrum $|\dot m(\omega)|^2$ of the cross-correlated pulse, as expected.

By construction, the finite-frequency traveltime distribution $\delta T(q)$ in eqs (46)–(47) and the recovered slowness anomaly $\delta\hat\sigma(r)$ in eqs (54)–(55) are an Abel transform pair:

$$\delta T(q) = \int_{-\infty}^\infty \delta\hat\sigma(\sqrt{q^2+l^2})\,dl = 2\int_q^\infty \frac{r\,\delta\hat\sigma(r)\,dr}{\sqrt{r^2-q^2}} = \delta\hat\sigma_{\rm A}(q), \tag{56}$$

$$\delta\hat\sigma(r) = -\frac{1}{\pi}\int_r^\infty \frac{\delta T'(q)\,dq}{\sqrt{q^2-r^2}}. \tag{57}$$

Eqs (56) and (57) assert that $\delta T(q)$ is the ray-theoretical traveltime residual through the blunted and blurred anomaly $\delta\hat\sigma(r)$. Attempts to verify these forward-inverse relations directly, or to determine $\delta T_{\rm A}(p)$ directly from the defining relation (eq. 48), lead to apparently intractable integrations. The initial integration over all rays $-\infty \le m \le \infty$ in eq. (49) seems to be the key to the simplification, enabling the derivation of the explicit $\delta\sigma(r) \to \delta\hat\sigma(r)$ relation (eqs 54–55).

4.5 Conservation of mass and area

The total mass of the recovered spherically symmetric anomaly $\delta\hat\sigma(r)$ is

$$4\pi\int_0^\infty r^2\delta\hat\sigma(r)\,dr = 4\pi\int_0^\infty r^2\,dr\int_0^\infty G(r,r')\,\delta\sigma(r')\,dr'. \tag{58}$$

The integral over r can be evaluated following an interchange in the order of integration:

$$\int_0^\infty r^2 G(r,r')\,dr = r'^2, \tag{59}$$

so that eq. (58) reduces to the conservation relation

$$4\pi\int_0^\infty r^2\delta\hat\sigma(r)\,dr = 4\pi\int_0^\infty r^2\delta\sigma(r)\,dr. \tag{60}$$

The cross-sectional area of the circularly-symmetric, finite-frequency traveltime distribution $\delta T(q)$ in the receiver plane is

$$2\pi\int_0^\infty q\,\delta T(q)\,dq = 4\pi\int_0^\infty dq\,q\int_q^\infty \frac{r\delta\hat\sigma(r)\,dr}{\sqrt{r^2-q^2}} = 4\pi\int_0^\infty r^2\delta\hat\sigma(r)\,dr, \tag{61}$$

Downloaded from https://academic.oup.com/gji/article/157/1/315/558524 by guest on 22 September 2022

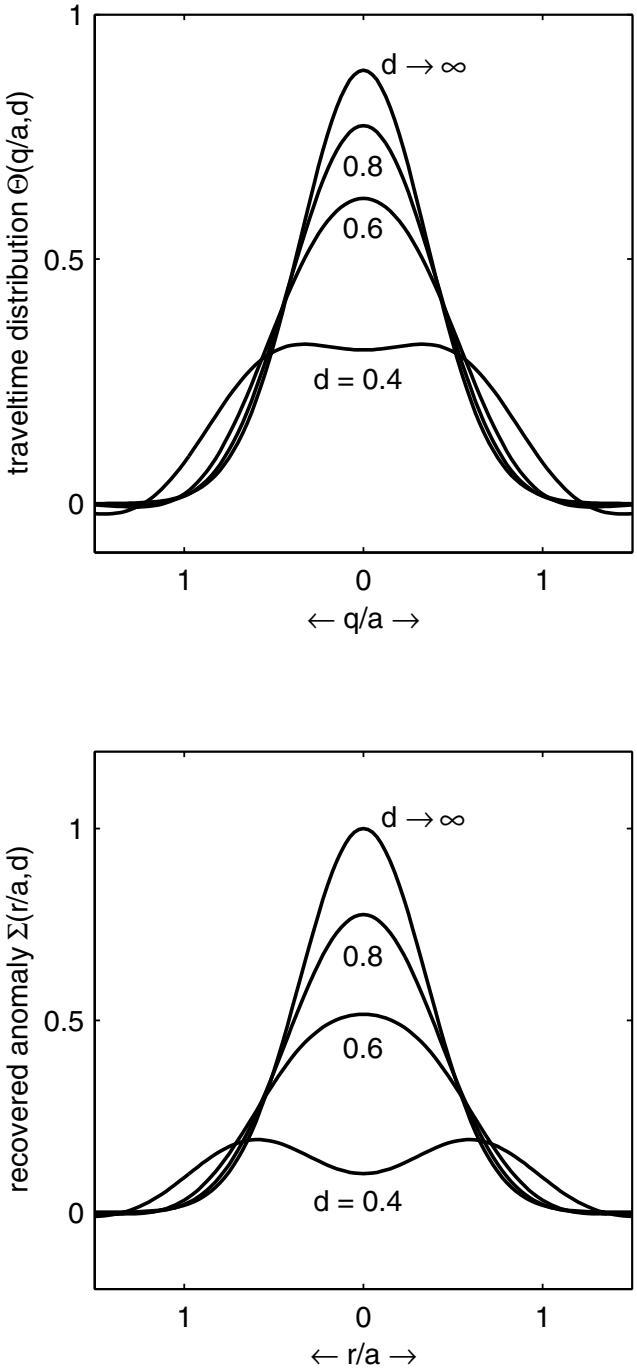

Figure 7. (Top) Cross-section through the dimensionless traveltime distribution $\Theta(q/a, d)$ for doughnut-hole parameters $d = 0.4$, 0.6, 0.8 and $d \to \infty$. (Bottom) Cross-section through the dimensionless slowness anomaly $\Sigma(q/a, d)$ for the same doughnut-hole parameters. All plots have been mirrored so that q/a and r/a increase from the center in both directions. The limiting ray-theoretical profiles are given by $\Theta(q/a, \infty) = \frac{1}{2}\sqrt{\pi}\exp(-4r^2/a^2)$ and $\Sigma(r/a, \infty) = \exp(-4r^2/a^2)$.

where we have made use of eq. (56) and then followed the same argument used to derive eq. (41) to obtain the first and second relations, respectively. Combining eqs (60) and (61) we obtain a fourfold identity:

$$4\pi \int_0^\infty r^2 \delta\hat{\sigma}(r)\, dr = 4\pi \int_0^\infty r^2 \delta\sigma(r)\, dr$$
$$= 2\pi \int_0^\infty q\,\delta T(q)\, dq = 2\pi \int_0^\infty q\,\delta T_{\rm ray}(q)\, dq. \tag{62}$$

This result stipulates that both the total mass of a recovered anomaly and the total traveltime area are independent of the frequency content $|\dot{m}(\omega)|^2$ of the probing wave.

Downloaded from https://academic.oup.com/gji/article/157/1/315/558524 by guest on 22 September 2022

4.6 Example: Gaussian sphere

We illustrate the results in Sections 4.4 and 4.5 by considering the simple case of a Gaussian slowness distribution:

$$\delta\sigma(r) = \exp(-4r^2/a^2), \tag{63}$$

where a pre-multiplier with the proper units of time/length is understood. We shall refer to the quantity a as the characteristic diameter of the slow sphere. The ray-theoretical traveltime distribution in the wake of such a Gaussian sphere is also a Gaussian:

$$\delta T_{\rm ray}(q) = \frac{1}{2}\sqrt{\pi}\, a \exp(-4r^2/a^2). \tag{64}$$

For any pulse power spectrum $|\dot{m}(\omega)|^2$ and any spherically-symmetric slowness anomaly $\delta\sigma(r)$, the recovered anomaly (eq. 54) and the finite-frequency traveltime distribution (eq. 56) may be written in dimensionless form as

$$\delta\hat{\sigma}(r) = \Sigma(r/a, d), \qquad \delta T(q) = a\Theta(q/a, d), \tag{65}$$

where $d = a/\sqrt{\lambda L}$ is the doughnut-hole parameter defined in eq. (14). Expressions for the dimensionless functions $\Theta(r/a, d)$ and $\Sigma(q/a, d)$ are derived in Appendix A, for the case that $|\dot{m}(\omega)|^2$ is given by eq. (7) and $\delta\sigma(r)$ is given by eq. (63).

Plots of the recovered anomaly $\delta\hat{\sigma}(r)$ and the traveltime distribution $\delta T(q)$, obtained by numerical evaluation of eqs (A3) and (A5), are illustrated in Fig. 7. Both $\delta\hat{\sigma}(r)$ and $\delta T(q)$ reduce to the corresponding ray-theoretical values, given by eqs (63) and (64), in the limit $d \to \infty$. As the doughnut-hole parameter d is reduced, $\delta\hat{\sigma}(r)$ and $\delta T(q)$ exhibit a reduction in their maximum magnitude, combined with a less dramatic lateral spreading. For doughnut-hole parameters less than $d \approx 0.5$, the maximum of the recovered anomaly $\delta\hat{\sigma}(r)$ no longer occurs at the center of the sphere, $r = 0$; instead, $\delta\hat{\sigma}(r)$ exhibits a local minimum at $r = 0$, surrounded by a spherically-symmetric maximum that gradually moves out to $r \to \infty$ as $d \to 0$. The variation of the central and maximum slowness with doughnut-hole parameter d is shown in Fig. 8. The magnitude is reduced to half of its actual value, $\delta\hat{\sigma}(0) = \delta\hat{\sigma}_{\rm max} = 0.5$ at a value $d \approx 0.6$. For doughnut-hole parameters less than $d \approx 0.3$, the core of the recovered anomaly is negative, $\delta\hat{\sigma}(0) < 0$.

4.7 Point spread function

We consider next a slowness anomaly that is a 3-D Dirac delta distribution:

$$\delta\sigma(r) = \frac{\delta(r)}{4\pi r^2}, \tag{66}$$

where a pre-multiplier with the proper units, in this case time $\times$ (length)^2, is understood. We denote the recovered image and the associated finite-frequency traveltime distribution corresponding to eq. (66) by

$$\delta\hat{\sigma}(r) = S(r), \qquad \delta T(q) = \delta T_S(q). \tag{67}$$

Borrowing from the lexicon of optics and astronomy, we shall refer to the recovered Dirac delta image $S(r)$ as the point spread function. Upon inserting eq. (66) into the representation (eq. 54), we obtain

$$S(r) = \lim_{r' \to 0}\left[\frac{G(r, r')}{r'}\right]. \tag{68}$$

The limit in eq. (68) can be evaluated with the aid of l' Hôpital's rule:

$$S(r) = \left(\frac{2\sigma}{\pi L}\right)^{3/2} \frac{\int_0^\infty \omega^{7/2}|\dot{m}(\omega)|^2 \sin\left(\frac{2\omega\sigma}{L}r^2 - \frac{\pi}{4}\right) d\omega}{\int_0^\infty \omega^2|\dot{m}(\omega)|^2\, d\omega}. \tag{69}$$

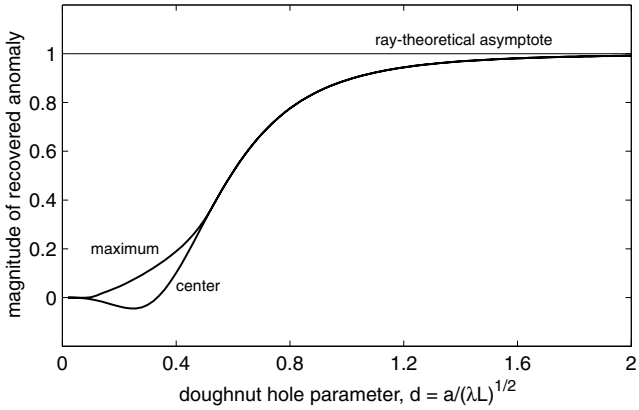

Figure 8. Variation of the central and maximum values of the recovered slowness anomaly $\delta\hat{\sigma}(r)$ as a function of the doughnut-hole parameter $d = a/\sqrt{\lambda L}$. The input anomaly $\delta\sigma(r)$ is a Gaussian sphere, of characteristic diameter a, given by eq. (63). In the ray-theoretical limit, the anomaly is fully recovered: $\delta\hat{\sigma}(0) = \delta\hat{\sigma}_{\rm max} \to 1$ as $d \to \infty$.

Downloaded from https://academic.oup.com/gji/article/157/1/315/558524 by guest on 22 September 2022

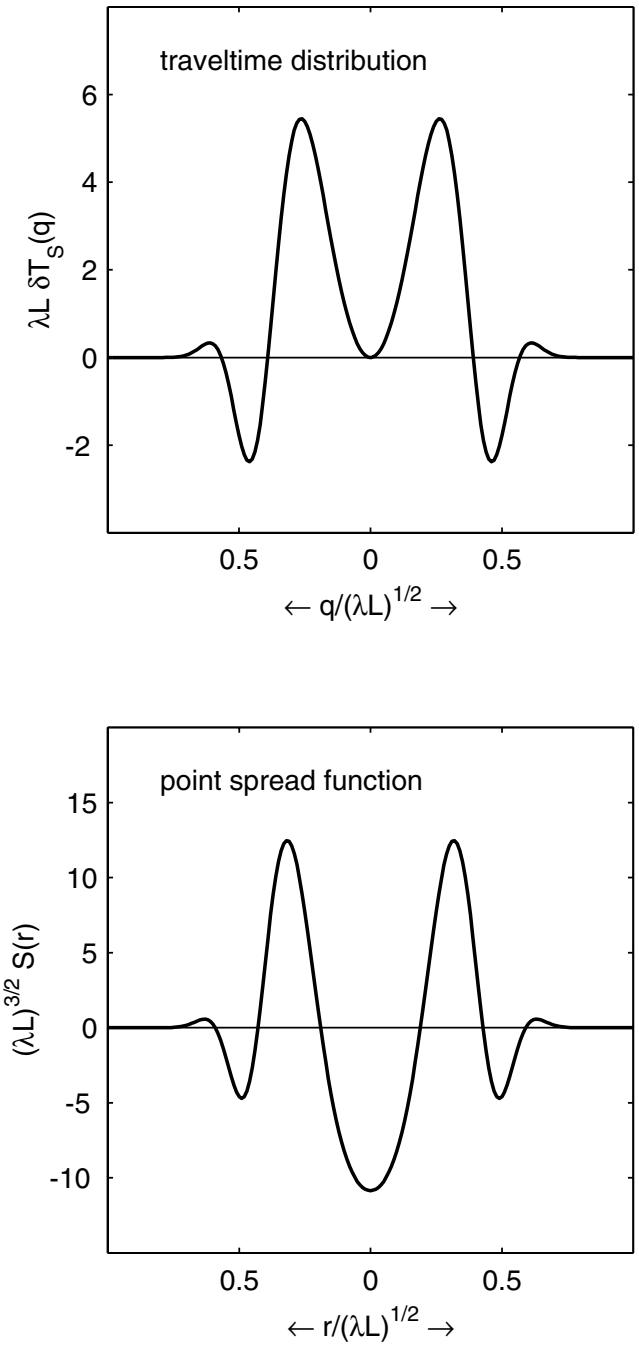

Figure 9. (Top) Cross-section through the dimensionless point spread traveltime distribution $\lambda L\ \delta T_S(q)$. (Bottom) Cross-section through the dimensionless point spread function $(\lambda L)^{3/2} S(r)$. Both plots have been mirrored so that $q/\sqrt{\lambda L}$ and $r/\sqrt{\lambda L}$ increase from the center in both directions. The source-pulse power spectrum $|\dot{m}(\omega)|^2$ is given by eq. (7). The shape of $\delta T_S(q)$ is identical to that of the finite-frequency sensitivity kernel $K(q)$, depicted in Fig. 2.

From eq. (42) we find (not surprisingly) that the associated traveltime distribution $\delta T_S(q)$ is identical to the cross-sectional shape of the sensitivity kernel, given in eq. (12):

$$\delta T_S(q) = \left(\frac{2\sigma}{\pi L}\right) \frac{\int_0^\infty \omega^3 |\dot{m}(\omega)|^2 \sin\left(\frac{2\omega\sigma}{L} q^2\right) d\omega}{\int_0^\infty \omega^2 |\dot{m}(\omega)|^2 \, d\omega}. \tag{70}$$

Dimensionless forms of eqs (69) and (70), suitable for numerical evaluation, are given in Appendix B. Cross-sectional plots of the point spread function $S(r)$ and associated traveltime distribution $\delta T_S(q)$ are displayed in Fig. 9. It is seen that a Dirac delta input is spread by a ray-theoretical inversion into a layered, spherically-symmetric slowness distribution of diameter $\sim \sqrt{\lambda L}$. The strongly oscillatory character of the recovered image $S(r)$ is particularly noteworthy: an interior core of negative slowness, $S(r) < 0$, is surrounded by a mantle of positive slowness, $S(r) > 0$, and a crust of negative, then positive, slowness.

Downloaded from https://academic.oup.com/gji/article/157/1/315/558524 by guest on 22 September 2022

5 ARBITRARY 3-D SLOWNESS ANOMALY

We return now to the general 3-D problem posed in Section 2 and illustrated in Fig. 1: what is the character of the recovered image $\delta\hat{\sigma}(\mathbf{x})$ in the case of a non-spherically-symmetric slowness anomaly $\delta\sigma(\mathbf{x})$?

5.1 Recovered image

Eq. (69) describes the finite-frequency spreading of a Dirac delta distribution (eq. 66) centered at the origin $\mathbf{x} = \mathbf{0}$. Subject to the premise that the anomaly $\delta\sigma(\mathbf{x})$ is small in extent, $a \ll L$, and situated approximately halfway between the source and receiver, $L' \approx L'' \approx L/2$, however, every point $\mathbf{x} \neq \mathbf{0}$ will be spread in exactly the same way. To find a general 3-D recovered image $\delta\hat{\sigma}(\mathbf{x})$, we simply need to convolve the input image $\delta\sigma(\mathbf{x})$ with the point spread function (eq. 69):

$$\delta\hat{\sigma}(\mathbf{x}) = \int\int\int_{-\infty}^{\infty} G(\mathbf{x}, \mathbf{x}')\, \delta\sigma(\mathbf{x}')\, d^3\mathbf{x}', \tag{71}$$

where

$$G(\mathbf{x}, \mathbf{x}') = \left(\frac{2\sigma}{\pi L}\right)^{3/2} \frac{\int_0^{\infty} \omega^{7/2} |\dot{m}(\omega)|^2 \sin\left(\frac{2\omega\sigma}{L}\|\mathbf{x} - \mathbf{x}'\|^2 - \frac{\pi}{4}\right) d\omega}{\int_0^{\infty} \omega^2 |\dot{m}(\omega)|^2 d\omega}. \tag{72}$$

Eqs (71–72) are the 3-D analogue of the spherically-symmetric $\delta\sigma(r) \rightarrow \delta\hat{\sigma}(r)$ relations (54)–(55); the point spread function $G(\mathbf{x}, \mathbf{x}') = S(\|\mathbf{x} - \mathbf{x}'\|)$ is the 3-D finite-frequency blurring filter. In the case of a spherically-symmmetric slowness anomaly (eq. 36), the 3-D integral (eq. 71) reduces to

$$\delta\hat{\sigma}(r) = \left(\frac{2\sigma}{\pi L}\right)^{3/2} \frac{2\pi}{N} \int_0^{\pi} d\theta \sin\theta \int_0^{\infty} dr' r'^2 \delta\sigma(r') \int_0^{\infty} d\omega\, \omega^{7/2} |\dot{m}(\omega)|^2 \sin\left[\frac{2\omega\sigma}{L}(r^2 + r'^2 - rr'\cos\theta) - \frac{\pi}{4}\right], \tag{73}$$

where $r = \|\mathbf{x}\|$, $r' = \|\mathbf{x}'\|$, $\cos\theta = (\mathbf{x} \cdot \mathbf{x}')/rr'$, and N is the normalization integral defined in eq. (13). Upon interchanging the order of integration and evaluating the integral over θ in eq. (73), we find that eqs (71–72) are consistent with eqs (54–55), as of course they must be.

5.2 Conservation of mass redux

The point spread function $S(r)$ and associated finite-frequency traveltime distribution $\delta T_S(q)$ satisfy the spherically symmetric mass and area conservation eqs (62):

$$4\pi \int_0^{\infty} r^2 S(r)\, dr = 2\pi \int_0^{\infty} q\, \delta T_S(q)\, dq = 1. \tag{74}$$

Because a volumetric integral over all of space is unaffected by a translation, the 3-D point spread filter (eq. 72) must satisfy

$$\int\int\int_{-\infty}^{\infty} G(\mathbf{x}, \mathbf{x}')\, d^3\mathbf{x} = 1. \tag{75}$$

Upon integrating eq. (71) over $\mathbf{x}$ and exploiting the identity (eq. 75), we obtain the 3-D generalization of the conservation of mass law (eq. 60):

$$\int\int\int_{-\infty}^{\infty} \delta\hat{\sigma}(\mathbf{x})\, d^3\mathbf{x} = \int\int\int_{-\infty}^{\infty} \delta\sigma(\mathbf{x})\, d^3\mathbf{x}. \tag{76}$$

Wave front healing and other finite-frequency effects will generally give rise to both a lateral spreading and a reduction in the maximum amplitude of a recovered anomaly $\delta\hat{\sigma}(\mathbf{x})$. The 3-D conservation law (eq. 76) guarantees that the spreading will always be a less significant effect than the amplitude reduction; roughly speaking, we must have

$$\frac{\hat{a}}{a} \sim \left(\frac{\delta\hat{\sigma}_{\max}}{\delta\sigma_{\max}}\right)^{-1/3}, \tag{77}$$

where $\delta\hat{\sigma}_{\max}$ and $\hat{a}$ are the maximum magnitude and the characteristic linear dimension of the recovered image, respectively. The blunted and blurred 1-D Gaussian profiles $\delta\hat{\sigma}(r)$ in Fig. 5 are consistent with the rule-of-thumb (eq. 77). In actual tomographic studies, with imperfect geographical coverage, the image magnitude $\delta\hat{\sigma}_{\max}$ and dimension $\hat{a}$ will be affected by the damping and/or smoothing used to regularize the inversion, as well as by finite-frequency effects; the conservation of mass law (eq. 76) strictly applies only in the limit of ideal ray coverage and negligible damping and smoothing.

5.3 Examples

We illustrate the 3-D result (eqs 71–72) with two examples. The first is a 3-D dumbbell composed of two Gaussian spheres of characteristic diameter a, offset from each other by a distance $b = \|\mathbf{b}\|$:

$$\delta\sigma(\mathbf{x}) = \frac{1}{2}\left[\exp\left(-4\left\|\mathbf{x} - \frac{1}{2}\mathbf{b}\right\|^2/a^2\right) + \exp\left(-4\left\|\mathbf{x} + \frac{1}{2}\mathbf{b}\right\|^2/a^2\right)\right]. \tag{78}$$

Downloaded from https://academic.oup.com/gji/article/157/1/315/558524 by guest on 22 September 2022

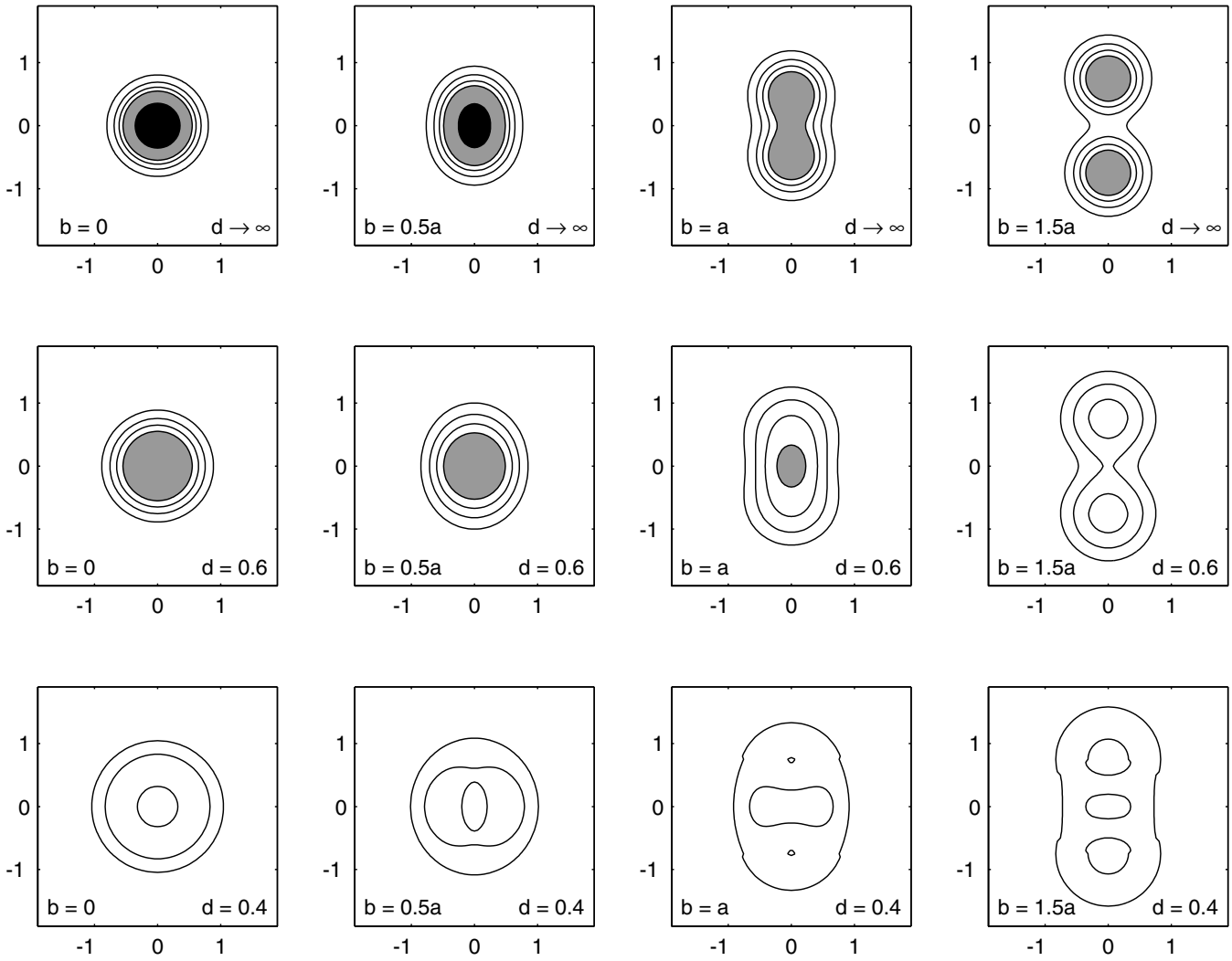

Figure 10. (Top row) Axial cross-sections through a 3-D superposition (eq. 78) of two vertically aligned Gaussian spheres, separated by distances $b = 0$, $b = 0.5a$, $b = a$ and $b = 1.5a$ (left to right). Contours of perturbed slowness $\delta\sigma(\mathbf{x})$ are plotted at 0.075, 0.15, 0.225, 0.3 and 0.6; gray stippling denotes regions where $0.3 < \delta\sigma(\mathbf{x}) < 0.6$; black denotes regions where $\delta\sigma(\mathbf{x}) > 0.6$. (Middle row) Corresponding recovered images (eq. 79) for doughnut-hole parameter $d = a/\sqrt{\lambda L} = 0.6$. (Bottom row) Recovered images $\delta\hat{\sigma}(\mathbf{x})$ for $d = 0.4$. The same irregular contouring scheme is used to plot $\delta\hat{\sigma}(\mathbf{x})$; the closer spacing near zero perturbed slowness enables details of the subdued images $\delta\hat{\sigma}(\mathbf{x})$ to be seen.

The recovered anomaly $\delta\hat{\sigma}(\mathbf{x})$ is a similar superposition of two blurred Gaussian spheres:

$$\delta\hat{\sigma}(\mathbf{x}) = \frac{1}{2}\left[\Sigma\left(\left\|\mathbf{x} - \frac{1}{2}\mathbf{b}\right\|/a, d\right) + \Sigma\left(\left\|\mathbf{x} + \frac{1}{2}\mathbf{b}\right\|/a, d\right)\right]. \tag{79}$$

In the limit $b = 0$, eqs (78) and (79) reduce to the single-sphere results in eqs (63) and (65). Axial cross-sections through the input ($d \to \infty$) dumbbell $\delta\sigma(\mathbf{x})$ are illustrated in Fig. 10 for various offsets $b = 0$, $b = 0.5a$, $b = a$ and $b = 1.5a$. The recovered dumbbell is also shown for two values of the doughnut-hole parameter, $d = a/\sqrt{\lambda L} = 0.6$ and $d = 0.4$. The recovered images are spread laterally and diminished in magnitude, in accordance with the rule-of-thumb (eq. 77). The blunting and blurring become increasingly pronounced as the doughnut-hole parameter d is decreased: the side-lobes of the 3-D point spread function $G(\mathbf{x}, \mathbf{x}') = S(\|\mathbf{x} - \mathbf{x}'\|)$ conspire to produce three, weak, vertically aligned blobs rather than two, in both the $b = a$, $d = 0.4$ and the $b = 1.5a$, $d = 0.4$ cross-sections.

Our second example is a superposition of 92 Gaussian spheres (eq. 63), arrayed in a plane to form the five-letter word PLUME. The input ($d \to \infty$) image $\delta\sigma(\mathbf{x})$ and the recovered images $\delta\hat{\sigma}(\mathbf{x})$ for doughnut-hole parameters $d = 0.6$ and $d = 0.4$ are shown in Fig. 11. The $d = 0.6$ image is blurred but still recognizable; however, upon viewing the $d = 0.4$ image, a skeptic (perhaps from Caltech) might conclude that this particular PLUME, and perhaps many others, did not exist.

6 DISCUSSION

Sheng & Schuster (2003) have recently presented an analysis of the finite-frequency limit of traveltime tomography that is more general than ours, in as much as they explicitly allow for the possibility of an irregular and incomplete source-receiver distribution and an arbitrary

Downloaded from https://academic.oup.com/gji/article/157/1/315/558524 by guest on 22 September 2022

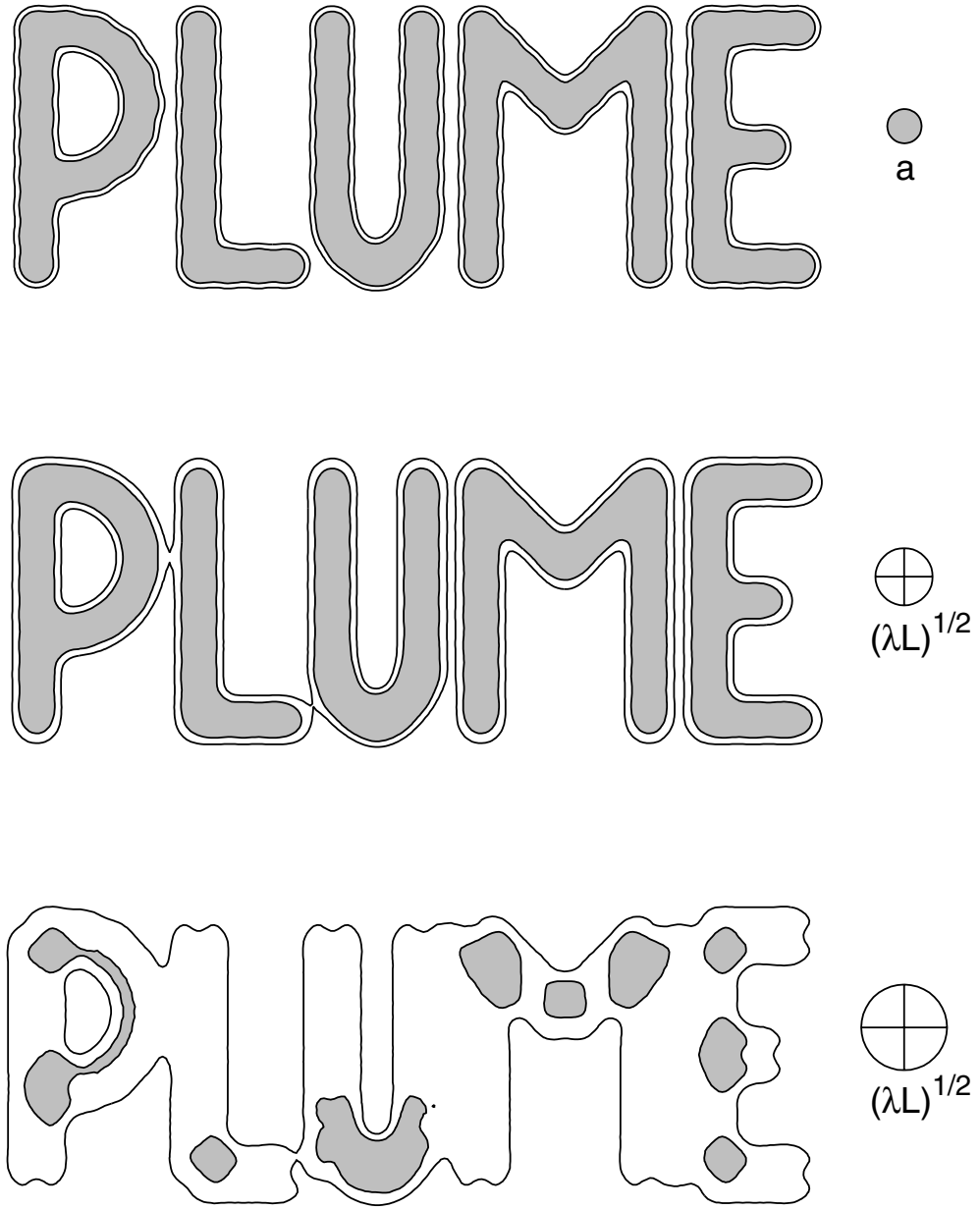

Figure 11. (Top) Superposition of 92 Gaussian spheres arrayed in a plane to form the word PLUME. Contours of perturbed slowness $\delta\sigma(\mathbf{x})$ are plotted at 0.4 and 0.6; gray stippling denotes regions where $\delta\sigma(\mathbf{x}) > 0.6$. The characteristic diameter a of a constituent sphere is shown on the right. (Middle) Corresponding recovered image $\delta\hat{\sigma}(\mathbf{x})$ for a doughnut-hole parameter $d = a/\sqrt{\lambda L} = 0.6$. (Bottom) Recovered image $\delta\hat{\sigma}(\mathbf{x})$ for $d = 0.4$. The same contouring scheme is used to plot $\delta\hat{\sigma}(\mathbf{x})$. Bull's-eyes on right show the characteristic diameter $\sqrt{\lambda L}$ of the finite-frequency point spread filter $G(\mathbf{x}, \mathbf{x}')$.

background slowness distribution, $\sigma(\mathbf{x}) \neq$ constant. They derive a $\delta\sigma(\mathbf{x}) \rightarrow \delta\hat{\sigma}(\mathbf{x})$ relationship in the form of eq. (71) in which the point spread function $G(\mathbf{x}, \mathbf{x}')$ is expressed as a symbolic 3-D integration over a 'domain determined by the frequency range and by those source-receiver pairs for which the associated wave path and the recorded traveltimes can be influenced by the perturbation at $\mathbf{x}$.' They seek to determine only the approximate 3-D extent of the point spread function $G(\mathbf{x}, \mathbf{x}')$, presenting a number of examples, in which the spreading is influenced not only by finite-frequency effects, but also by well-known undersampling effects, which lead to streaking in the direction of any particularly well-populated family of rays. In this paper, we have assumed that the tomographic coverage is perfect, in order to isolate the effects of finite-frequency wave front healing. This simplification has enabled us to derive a much more explicit relation between the recovered and input images, $\delta\hat{\sigma}(\mathbf{x})$ and $\delta\sigma(\mathbf{x})$. Our restriction to a homogeneous background medium is not a fundamental limitation because the rays passing through a point $\mathbf{x}$ in a more general background medium may be considered to be locally straight: indeed, that is the basis of the so-called generalized Radon transform (Beylkin 1985; Miller *et al.* 1987), which is the starting point of the analysis by Sheng & Schuster (2003).

Downloaded from https://academic.oup.com/gji/article/157/1/315/558524 by guest on 22 September 2022

7 ANTIBLURRING R_X

In principle, the correct slowness perturbation $\delta\sigma(\mathbf{x})$ could be reconstructed from a blunted and blurred image $\delta\hat{\sigma}(\mathbf{x})$ by deconvolution with the 3-D point spread function $G(\mathbf{x}, \mathbf{x}')$. In the presence of traveltime measurement errors and imperfect ray coverage, this would be a highly dubious undertaking in as much as it would be plagued by instabilities induced by the strong oscillatory layering of $G(\mathbf{x}, \mathbf{x}')$, displayed in Fig. 9. It is preferable to use 3-D Fréchet sensitivity kernels $K(\mathbf{x})$ to account for finite-frequency wave front healing effects directly in the tomographic inversion, as done recently by Montelli *et al.* (2004a,b). Noise and limited ray sampling will always act to degrade seismic tomographic images $\delta\hat{\sigma}(\mathbf{x})$, however, the blunting and blurring resulting from finite-frequency diffraction effects can be easily accounted for.

ACKNOWLEDGMENTS

Conversations with Guust Nolet have, as always, been extremely stimulating. The originally submitted manuscript was improved by the thoughtful and constructive reviews of Colin Thomson and Jean Virieux. Financial support for this work has been provided by the US National Science Foundation under Grant EAR-0105387.

REFERENCES

Ahmad, B. & Tyler, G.L., 1998. The two-dimensional resolution kernel associated with retrieval of ionospheric and atmospheric refractivity profiles by Abelian inversion of radio occultation phase data, *Radio Science,* **33,** 129–142.

Baig, A.M. & Dahlen, F.A., 2004. Statistics of traveltimes and amplitudes in random media, *Geophys. J. Int.*, in press.

Baig, A.M., Dahlen, F.A. & Hung, S.-H., 2003. Traveltimes of waves in 3-D random media, *Geophys. J. Int.,* **153,** 467–482.

Beylkin, G., 1985. Imaging of discontinuities in the inverse scattering problem by inversion of a causal generalized Radon transform, *J. Math. Phys.,* **26,** 99–108.

Bracewell, R., 1965. *The Fourier Transform and its Applications*, McGraw-Hill, New York, pp. 262–266.

Dahlen, F.A., Hung, S.-H. & Nolet, G., 2000. Fréchet kernels for finite-frequency traveltimes—I. Theory, *Geophys. J. Int.,* **141,** 157–174.

Hung, S.-H., Dahlen, F.A. & Nolet, G., 2001. Wave front healing: a banana-doughnut perspective, *Geophys. J. Int.,* **146,** 289–312.

Miller, D., Oristaglio, M., & Beylkin, G., 1987. A new slant on seismic imaging: Migration and integral geometry, *Geophysics,* **52,** 943–964.

Montelli, R., Nolet, G., Masters, G., Dahlen, F.A. & Hung, S.-H., 2004b. Global P and PP traveltime tomography: rays versus waves, *Geophys. J. Int.*, in press.

Montelli, R., Nolet, G., Dahlen, F.A., Masters, G., Engdahl, E.R. & Hung, S.-H., 2004a. Finite-frequency tomography reveals a variety of plumes in the mantle, *Science,* **303,** 338–343.

Morse, P.M & Ingard, K.U., 1968. *Theoretical Acoustics*, McGraw-Hill, New York, pp. 306–332.

Sheng, J. & Schuster, G.T., 2003. Finite-frequency resolution limits of wave path traveltime tomography for smoothly varying velocity models, *Geophys. J. Int.,* **152,** 669–676.

Zhao, L., Jordan, T.H. & Chapman, C.H., 2000. Three-dimensional Fréchet kernels for seismic delay times, *Geophys. J. Int.,* **141,** 558–576.

APPENDIX A: GAUSSIAN GRUNGE

For completeness, we present the formulae used to compute the recovered image and finite-frequency traveltime distribution,

$$\delta\hat{\sigma}(r) = \Sigma(r/a, d), \qquad \delta T(q) = a\Theta(q/a, d), \tag{A1}$$

for the case

$$\delta\sigma(r) = \exp(-4r^2/a^2), \qquad |\dot{m}(\omega)|^2 = (\omega^2\sigma^2\lambda^2/2\pi)\exp(-\omega^2\sigma^2\lambda^2/4\pi^2), \tag{A2}$$

discussed in Section 4.6. The dimensionless slowness anomaly $\Sigma(r/a, d)$ can be found by substituting eqs (A2) into eq. (54) and evaluating the integral over r'. We obtain, after a lengthy calculation,

$$\begin{aligned}\Sigma(r/a, d) = {} & \frac{d}{2}\left(\int_0^\infty u^4 e^{-u^2/4\pi^2}\,du\right)^{-1}\int_0^\infty u^{9/2}e^{-u^2/4\pi^2}e^{-4Br^2/a^2} \\ & \times\left[(BA_+ + CA_-)\cos(4Cr^2/a^2 - \pi/4) + (CA_+ - BA_-)\sin(4Cr^2/a^2 - \pi/4)\right]du,\end{aligned} \tag{A3}$$

where

$$A_\pm = \left(\frac{\sqrt{1 + \frac{1}{4}d^4u^2} \pm 1}{1 + \frac{1}{4}d^4u^2}\right)^{1/2}, \qquad B = \frac{\frac{1}{4}d^4u^2}{1 + \frac{1}{4}d^4u^2}, \qquad C = \frac{\frac{1}{2}d^2u}{1 + \frac{1}{4}d^4u^2}. \tag{A4}$$

To determine the dimensionless traveltime distribution $\Theta(q/a, d)$, it is most convenient to return to the original 3-D integration in eq. (42) and evaluate the integrals over the Cartesian coordinates y, x and z in that order. Another lengthy calculation leads to

$$\Theta(q/a, d) = \frac{\sqrt{\pi}}{2}\left(\int_0^\infty u^4 e^{-u^2/4\pi^2}\,du\right)^{-1}\int_0^\infty u^4 e^{-u^2/4\pi^2}e^{-4Bq^2/a^2}\left[C\sin(4Cq^2/a^2) + B\sin(4Cq^2/a^2)\right]du. \tag{A5}$$

The remaining integrals over the dimensionless frequency $u = \omega\sigma\lambda$ in eqs (A3) and (A5) have been evaluated numerically to plot the results shown in Figs 5 and 8. In the ray-theoretical limit, $d \to \infty$, eqs (A3) and (A5) reduce to

$$\Sigma(r/a, \infty) = \exp(-4r^2/a^2), \qquad \Theta(q/a, \infty) = \frac{1}{2}\sqrt{\pi}\exp(-4q^2/a^2). \tag{A6}$$

The consistency of the above results with the mass and area conservation laws (eq. 62) can be verified by direct analytical integration.

Downloaded from https://academic.oup.com/gji/article/157/1/315/558524 by guest on 22 September 2022

APPENDIX B: POINT SPREAD STUFF

The point spread function (eq. 69) and associated finite-frequency traveltime distribution (eq. 70) can be written in dimensionless form as

$$S(r) = \left(\frac{2}{\pi\lambda L}\right)^{3/2} \frac{\int_0^\infty u^{11/2} e^{-u^2/4\pi^2} \sin\left(\frac{2r^2}{\lambda L}u - \frac{\pi}{4}\right) du}{\int_0^\infty u^4 e^{-u^2/4\pi^2}\, du}, \tag{B1}$$

$$\delta T_S(q) = \left(\frac{2}{\pi\lambda L}\right) \frac{\int_0^\infty u^5 e^{-u^2/4\pi^2} \sin\left(\frac{2q^2}{\lambda L}u\right) du}{\int_0^\infty u^4 e^{-u^2/4\pi^2}\, du}, \tag{B2}$$

where it has been assumed that $|\dot{m}(\omega)|^2 = (\omega^2\sigma^2\lambda^2/2\pi)\exp(-\omega^2\sigma^2\lambda^2/4\pi^2)$. It is evident that $S(r)$ is of the form $(\lambda L)^{-3/2} \times$ (a dimensionless function of $r/\sqrt{\lambda L}$), whereas $\delta T_S(q)$ is of the form $(\lambda L)^{-1} \times$ (a dimensionless function of $q/\sqrt{\lambda L}$). The integrals over dimensionless frequency $u = \omega\sigma\lambda$ have been evaluated numerically to plot the curves in Fig. 9.

Downloaded from https://academic.oup.com/gji/article/157/1/315/558524 by guest on 22 September 2022